

Article

Investigation of Optimal Coupling Velocities of the Sample and Sheath Flows for Hydrodynamic Focusing

Dingpeng Huang¹, Hangzhou Wang^{1,*} , Xiaoping Wang¹, Kan Guo¹, Zhuoli Yuan²,
Jiawang Chen¹  and Ying Chen¹ 

¹ Ocean College, Zhejiang University, Zhoushan 316021, China; huangdingpeng@zju.edu.cn (D.H.); xpwang@zju.edu.cn (X.W.); 21934156@zju.edu.cn (K.G.); arwang@zju.edu.cn (J.C.); ychen@zju.edu.cn (Y.C.)

² Polar Research Institute of China, Shanghai 200136, China; yuanzhuoli@pric.org.cn

* Correspondence: hangzhouwang@zju.edu.cn

Received: 6 July 2020; Accepted: 5 August 2020; Published: 12 August 2020



Abstract: Focusing performance is a major concern for systems based on hydrodynamic focusing. In this study, the hydrodynamic focusing subsystem of a microscopic imaging system was analysed and modelled. The theoretical model was used to analyse the velocity and distribution range of sample particles in the focused sample flow in the micro-channel of the hydrodynamic focusing subsystem, when the velocities of the sample and sheath flows were varied. The results were used to optimise the coupling velocities of the sample and sheath flows for the microscopic imaging system, to keep working efficiency and image quality of the system simultaneously. An independent experiment was then conducted for verification, and the results agreed well with the theoretical investigation. The results of this study provide a general framework for adjusting the sample and sheath flow velocities to optimise the hydrodynamic focusing performance.

Keywords: hydrodynamic focusing; optimal coupling velocity; sample flow; sheath flow; micro-channel

1. Introduction

Microfluidic focusing is used to arrange particles randomly distributed in fluid samples (e.g., water, blood) and it has been widely applied in many fields, such as biology, clinical research, and oceanology [1]. In flow cytometry, microfluidic focusing is used for counting, analysing, and sorting biological particles. Microfluidic focusing methods include electro-kinetic [2,3], acoustic [4], and hydrodynamic focusing [5]. Hydrodynamic focusing is based on fluid dynamics and offers two advantages over the other two methods: it does not need external forces (e.g., electro-kinetic, acoustic) or special requirements for the sample particles or fluids, which simplifies the system complexity [6], and it can operate effectively at a high flow rate to achieve a high throughput. These advantages indicate that hydrodynamic focusing can be used to develop highly efficient and inexpensive micro-flow cytometers [7].

In a hydrodynamic focusing system, the sample flow is generally enclosed and focused by the outer sheath flow to form a sample flow core, which passes through a predetermined area for further investigation. The characteristics (e.g., width, velocity) of the sample flow core, which significantly determine the system performance, mainly depend on the hydrodynamic characteristic of the flows in the system, microstructure of the flow channel, etc. Some studies have focused on investigating the theoretical hydrodynamic mechanisms of fluids to optimise the sample flow core for different applications [8,9]. Wang et al. analysed the focusing force exerted on the sample flow and particles in the sample flow core and found that it included the flow-induced drag force and inertial lift force. They also developed an inertial microfluidic focusing chip that only uses the inertial lift force to focus sample particles into a single position [10]. Panwar et al. examined the focusing performance of their

microfluidic focusing chip at different Reynolds numbers (Re) and observed that the performance increased with Re [11]. Many other studies have considered the design or optimisation of flow channel microstructures [12,13]. Lee et al. designed a microfluidic focusing flow channel after numerically modelling the focusing effect of different structures and the relative flow rate between the sheath and sample flows [14]. They also examined the focusing performance of different types of micro-channels (including symmetric and asymmetric) with different aspect ratios, then proposed an analytical method for predicting the location and width of the sample flow core in different micro-channels [15]. John et al. presented a micro-channel with both curved and straight sections to realise microfluidic inertial focusing. They demonstrated that this channel could passively focus sample particles based on inertia without the assistance of a sheath fluid [16]. Zhao et al. modelled the focusing behaviour of a chip-based microfluidic hydrodynamic structure. They developed a novel structure to achieve an effective focusing performance at a high sample flow rate and reported that the difference in velocities of the sheath and sample flows should be minimised where they meet to prevent potential mixing [17].

A microscopic imaging system is currently in development that can autonomously collect images of phytoplankton 10–150 μm in size from water samples. This system has adopted hydrodynamic focusing to arrange disordered particles in the water sample and pass them through the predetermined imaging area in sequence at an appropriate velocity. The velocities of the sample and sheath flows are adjusted at the micro-channel inlet. However, previous studies have mostly considered focusing the sample flow into a single-particle stream or simply noted the range of flow rates employed by a hydrodynamic focusing system. To the best of our knowledge, no studies have tried to improve the system efficiency by optimising the coupling velocities of the sample and sheath flows. In this study, we analysed and modelled the hydrodynamic focusing subsystem of the microscopic imaging system. The changes in velocity and distribution of sample particles in the imaging area with the velocities of the sample and sheath flows were theoretically simulated to obtain the optimal coupling velocities of these flows. The theoretical results were compared with those of a laboratory experiment for validation.

2. System Overview

As shown in Figure 1, the microscopic imaging system is primarily composed of a hydrodynamic focusing subsystem and optical imaging subsystem. The former is used to arrange disordered particles in the water sample and pass them through the imaging area in sequence. The latter takes images of the particles as they pass through the imaging area.

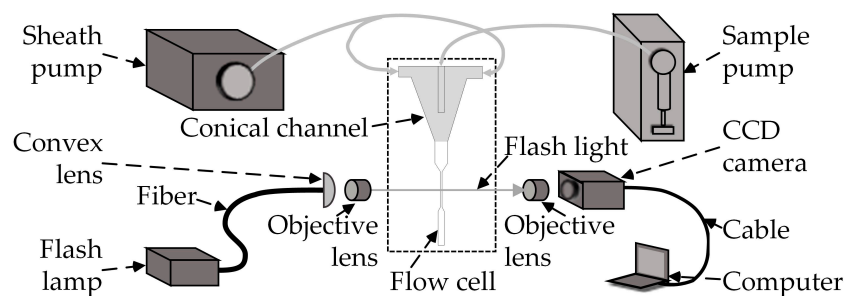


Figure 1. Schematic diagram of the configuration of the microscopic imaging system.

The hydrodynamic focusing subsystem comprises a sample pump, sheath flow pump, flow cell, and conical channel. A water sample is taken by the sample pump and then discharged very slowly via a fine needle at the central axis of the conical channel. A programmable syringe pump (ZSB-SY03, RUNZE Fluid Co., Ltd., Nanjing, Jiangsu, China) equipped with a 500 μL syringe was selected as the sample pump. The number of steps and speed of each step of the pump can be adjusted separately via a serial interface (i.e., RS-232 interface), which determines the flow rate of the pump from 0.142 $\mu\text{L/s}$ to 36.1 $\mu\text{L/s}$. At the outlet of the fine needle, the water sample is enclosed by a much faster outer

sheath fluid generated by the sheath flow pump. The sheath flow pump was a peristaltic pump (BT100-2J, Longer Precision Pump Co., Ltd., Baoding, Hebei, China) with a flow rate of 0.3–366.6 $\mu\text{L/s}$ and precision of 0.3 $\mu\text{L/s}$. The sheath flow aligns the particles of the injected water sample in sequence and keeps them in the centre. These particles enter the flow cell underneath the conical channel, and they are focused along the centre axis of the micro-channel, ideally. The silicon flow cell has a square micro-channel with a cross-section of $200 \times 200 \mu\text{m}$, which is wide enough to allow particles as large as $150 \mu\text{m}$ in diameter.

The optical imaging subsystem comprises a charge-coupled device (CCD) camera, a flash lamp, two objective lenses, and a convex lens. The CCD camera (GC1380H, Allied Vision Technologies Canada Inc., Burnaby, BC, Canada) is equipped with an objective lens having a magnification of $10\times$, and it is focused on the centre axis of the micro-channel (i.e., imaging area) to take images of the particles as they pass through. The camera has an image resolution of 1360×1024 pixels, and each pixel has a size of $6.45 \times 6.45 \mu\text{m}$. These dimensions were appropriate for our study because the target particles had a size of $10\text{--}150 \mu\text{m}$. The light emitted by the flash lamp (L9455-01, Hamamatsu Photonics Co., Ltd., Shizuoka, Japan) is guided by an optical fibre and is focused on the imaging area by the lens group (i.e., the combination of the objective lens and convex lens) to illuminate the imaging area. The flash lamp has a maximum repetition rate of 182 Hz and maximum input energy of 27.5 mJ per flash, which are vital to reducing the potential smear of particles in the images.

Because of the working mechanism of the system described above, particles in the micro-channel are always in motion. To take a clear image of these moving particles, two conditions need to be met. First, the particle should be within the depth of field (DOF) of the imaging device (i.e., the CCD camera and objective lens), which refers to the distance interval between the nearest and farthest objects sharply focused in an image. Second, the velocity of a particle in the imaging area should be optimised. An overly slow velocity reduces the working efficiency of the system, whereas an excessively fast velocity smears the particles in the image and reduces the imaging quality. The particle velocity is primarily determined by the velocities of the sample and sheath flows, geometry of the flow channel, etc. To ensure the working efficiency and image quality of the system, these two requirements must be satisfied simultaneously. We did this by optimising the coupling velocities of the sample and sheath flows via numerical modelling and validating the simulation results through a laboratory experiment.

3. Theoretical Optimisation of the Coupling Velocities

A theoretical model was built to represent the hydrodynamic focusing subsystem. Different combinations of the sample and sheath flow velocities were inputted to the model to investigate changes in the focusing performance (i.e., velocity and distribution range) of particles in the micro-channel and to determine the optimal coupling velocities of the sample and sheath flows.

3.1. Theoretical Model

As shown in Figure 2, a symmetric 3D model was adopted because the flow cell in the hydrodynamic focusing subsystem is symmetric and the conical channel is axisymmetric. These two parts were treated as a whole because they are tightly and physically connected. The model had two inlets and one outlet. One inlet was located at the axis of the conical channel to represent the entrance of the sample flow. It was surrounded by another inlet, which represented the entrance of the sheath flow. The outlet was placed at one end of the flow cell. Because the sample and sheath flows were independent, their velocities could be adjusted separately to examine the focusing performance. The relevant constants used in this model are listed in Table 1.

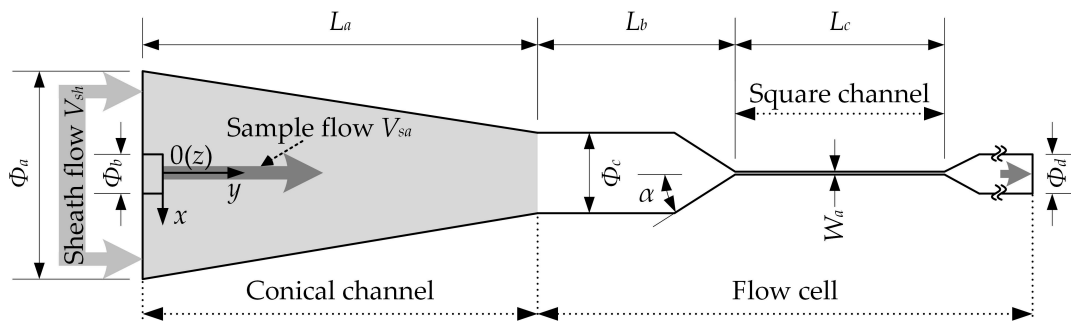


Figure 2. Cross sectional view of the theoretical model, indicating its geometric dimensions, inlet and outlet of the flows. Φ indicates diameter, L indicates length, and W indicates width.

Table 1. Constants adopted in the theoretical model.

Description	Expression	Description	Expression
L_a	9.9 mm	Φ_a	5.85 mm
L_b	5 mm	Φ_b	1 mm
L_c	5.75 mm	Φ_c	2 mm
α	30°	Φ_d	1 mm
W_a	0.2 mm		

In the micro-channel, the sample particle goes along the focused sample flow. To ensure a clear image of a moving particle, its motion in the micro-channel should be very stable and smooth; this requires laminar flow. Re was adopted as an indicator of laminar flow. It measures the ratio of inertial to viscous forces acting on particles flowing in a channel:

$$Re = \frac{\rho U_m D_h}{\mu}, \tag{1}$$

where ρ is the fluid density, μ is the coefficient of viscosity of the fluid, U_m is the maximum velocity of the fluid, and D_h is the hydraulic diameter of the channel. This can be expressed as

$$D_h = \frac{4A}{P_w} = W_a, \tag{2}$$

where A is the cross-sectional area of the channel, P_w is the wetted perimeter, and W_a is the channel width. By replacing D_h with Equation (2) and U_m with the maximum velocity V_{max} in the micro-channel, Equation (1) can be rewritten as

$$Re = \frac{\rho V_{max} W_a}{\mu}. \tag{3}$$

Two parameters were used to evaluate the focusing performance: the width of the focused sample flow W_{sa} and particle velocity V_p . Because the micro-channel had a laminar flow, the motion of the sample flow could be described via Navier–Stokes (N–S) equations. Three assumptions were used to investigate W_{sa} [15]:

1. The fluid is Newtonian. For a Newtonian fluid subjected to shear, the resulting strain rate ϵ_{xy} is linearly related to the applied stress τ_{xy} , which is numerically expressed as $\tau_{xy} = 2\mu\epsilon_{xy}$ [18].
2. The flow in the micro-channel is steady.
3. The density of the fluid in the channel is uniform.

Based on the above assumptions and theory of hydrodynamics, W_{sa} primarily depends on the width of the square micro-channel W_a and velocities of the sample flow V_{sa} and sheath flow V_{sh} .

According to the hydrodynamics principle, in a straight square channel (i.e., square channel in Figure 2), the velocity profile V of a fully developed laminar flow can be formulated as [19]

$$V = \frac{4W_a^2}{\mu\pi^3} \left(-\frac{dP}{dy} \right) \sum_{n=0}^{\infty} \frac{(-1)^n}{(2n+1)^3} \left\{ 1 - \frac{\cosh[(2n+1)\pi x/W_a]}{\cosh[(2n+1)\pi/2]} \right\} \cos \frac{(2n+1)\pi z}{W_a}, \quad (4)$$

where x, y, z are the coordinates (Figure 2), W_a is the channel width, and P is the pressure. In a laminar flow, the velocity is along the axial direction of the channel. In each cross-section of the square channel, the velocity gradually decreases from the maximum at the centre to zero at the inner surface of channel.

3.2. Theoretical Simulation

3.2.1. Parameters for Guiding and Evaluating the Theoretical Simulation

Two parameters were adopted to evaluate the results of the theoretical simulation: the DOF of the imaging device and optimal particle velocity V_{p_op} . For the optical imaging subsystem, the DOF can be calculated as

$$\text{DOF} = \frac{\lambda \cdot n}{NA^2} + \frac{p \cdot n}{M \cdot NA}, \quad (5)$$

where λ is the wavelength of light with a value of 550 nm, n is the refractive index of water and glass with a value of 2, and p is the pixel size of the CCD camera (i.e., 6.45 μm). NA and M are the numerical aperture and magnification, respectively, of the objective lens with values of 0.25 and 10, respectively. Thus, the DOF was calculated to be 22.76 μm .

V_{p_op} represents the critical particle velocity; above this value, the smear of the particle in the image collected by the CCD camera will be serious and unacceptable. Because there is no rigorous definition for calculating V_{p_op} , an empirical formula was adopted to approximate it. From Olson et al. [20], a smear of 7.5 pixels was thought to be acceptable for sample particle (i.e., beads) as small as 20 μm . In this study, since the size of the smallest sample particle (i.e., 10 μm) was half of 20 μm , a smear of 3.75 pixels was thought to be appropriate. Therefore,

$$3.75e = M \cdot t \cdot V_{p_op}, \quad (6)$$

Conversely,

$$V_{p_op} = \frac{3.75e}{M \cdot t}, \quad (7)$$

where e and t are the pixel size and exposure time of the camera, respectively. For the optical imaging subsystem, a flash lamp was used instead of the shutter of the CCD camera to control the exposure time because the emission pulse duration of the former (i.e., $\sim 1 \mu\text{s}$) was far shorter than the shutter duration of the camera (i.e., 10 μs). By substituting the values of 1 μs and 6.45 μm into t and e , respectively, in Equation (7), V_{p_op} was calculated to be 2 m/s.

3.2.2. Details of the Theoretical Simulation

We investigated the motion of particles in the micro-channel following the theoretical model in Section 3.1 by using COMSOL Multiphysics (COMSOL Inc.). The sheath and sample flows were modelled in the laminar flow regime and were considered incompressible. The sample flow velocity was modelled at five values from 1.8 mm/s to 9 mm/s, which corresponded to flow rates from 1.42 to 7.10 $\mu\text{L/s}$ of the sample pump. At each sample flow velocity, the sheath flow velocity was modelled at five values of 1, 1.5, 2, 3, and 4 mm/s, which corresponding to flow rates of 25.5, 38.2, 51.0, 76.5, and 102 $\mu\text{L/s}$ for the sheath flow pump. The velocities of the sample and sheath flows were selected to ensure that V_{p_op} was within the velocity range of particles in the micro-channel. Each sample particle with the same velocity was distributed at a grid point of the inlet. All particles were released simultaneously (i.e., $t = 0 \text{ s}$) at the beginning of the simulation to trace their range. Because the sample

flow and sheath flow velocities each had five test values, 25 groups of simulations were conducted in total. For each simulation, the particle distribution range and velocity and the flow velocity profile were recorded to evaluate the focusing performance of the hydrodynamic focusing subsystem. The relevant constants used in this simulation are listed in Table 2.

Table 2. Constants of the liquid and sample particles used in the theoretical simulation.

Description	Expression
Density (liquid)	$1 \times 10^3 \text{ kg/m}^3$
Viscosity (liquid)	$1 \times 10^{-3} \text{ Pa s}$
Density (particle)	1050 kg/m^3
Diameter (particle)	$1 \times 10^{-5} \text{ m}$
Temperature	293.15 K

3.3. Theoretical Simulation Results

3.3.1. Sample Particle Velocity V_p

In this study, the sample particle velocity V_p in the micro-channel primarily depended on the sample flow velocity V_{sa} and sheath flow velocity V_{sh} . To determine V_{p_opr} , we needed to evaluate how V_p is affected by V_{sa} and V_{sh} . We observed that the flow velocity V increased rapidly from the conical channel to the square micro-channel and remained almost steady for most of the micro-channel (Figure 3a). The flow velocity V in the micro-channel gradually decreased from the maximum value at the centreline (i.e., $x = 0, z = 0$) to zero at the inner surface of the channel in a parabolic manner (Figures 3b and 4), at each horizontal cross section the micro-channel. Therefore, a polynomial function could be adopted to represent V as a function of x by:

$$V(x) = ax^2 + bx + c, \tag{8}$$

where $a, b,$ and c are the least-squares fitted coefficients (Table 3). And the goodness of the fit indicated by R^2 are all better than 0.9715. These results agree with theoretical analysis in Section 3.1 and indicate that the micro-channel has a fully developed laminar flow [19]. The sample particles were closely focused around the central axis of the micro-channel (Figure 3c,d), which indicates that the hydrodynamic focusing subsystem functioned well. Meanwhile, the particle velocity was very close to the flow velocity in the micro-channel.

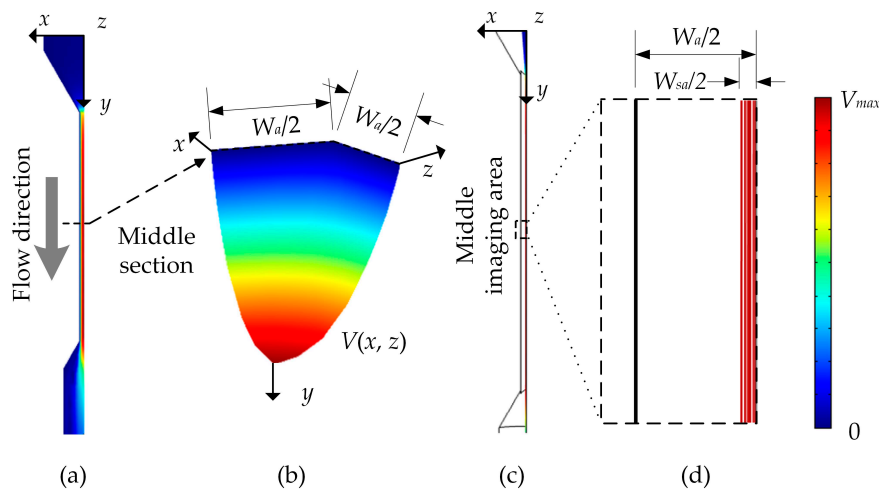


Figure 3. Flow velocity profile at (a) vertical cross section and (b) horizontal cross section of the micro-channel. Sample particle velocity profile at (c) side view and (d) the middle imaging area of the micro-channel.

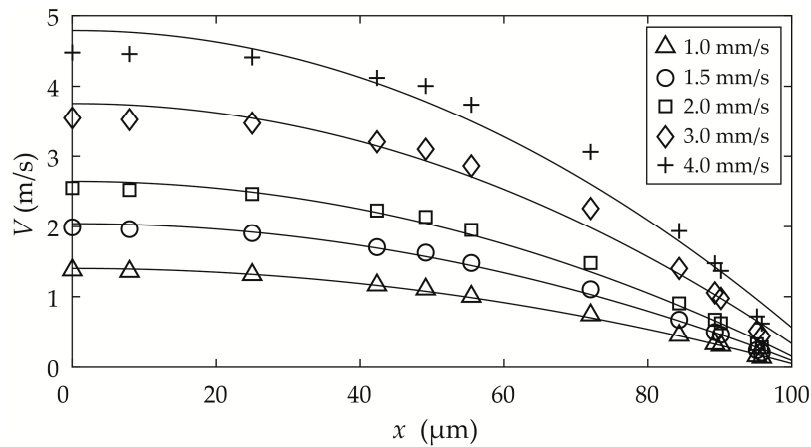


Figure 4. Flow velocity V as a function of x for five sheath flow velocities V_{sh} at the sample flow velocity V_{sa} of 1.8 mm/s.

Table 3. The fitted coefficients of flow velocity V versus x at five demonstrative sheath flow velocities V_{sh} at the sample flow velocity V_{sa} of 1.8 mm/s.

V_{sh} (mm/s)	a	b	c	R^2
1.0	-1.358×10^8	2.720×10^4	0.04044	0.9977
1.5	-1.956×10^8	3.920×10^4	0.07649	0.9977
2.0	-2.503×10^8	5.018×10^4	0.1286	0.9925
3.0	-3.448×10^8	6.923×10^4	0.2786	0.9826
4.0	-4.273×10^8	8.591×10^4	0.4718	0.9715

As noted above, the sample particle velocities across the cross-section of the micro-channel were very similar. To facilitate the analysis, we selected the particle velocity at the intersection of the central axis and middle cross-section of the micro-channel to represent V_p . Figure 5a shows that V_p increased linearly with V_{sh} for all values of V_{sa} . The increasing rate was very close for all V_{sa} values, but the intercept increased with V_{sa} . Therefore, a linear function was adopted to represent V_p as a function of V_{sh} at each V_{sa} :

$$V_p(V_{sh}) = a_{sh} V_{sh} + b_{sh}, \tag{9}$$

where a_{sh} and b_{sh} are the least-squares fitted slope and intercept, respectively. The goodness of each fit was better than 0.9999 (Table 4). V_p also increased in a strongly linear manner with increasing V_{sa} at each V_{sh} , as shown in Figure 5b. Thus, we fitted a linear relationship to V_p and V_{sa} :

$$V_p(V_{sa}) = a_{sa} V_{sa} + b_{sa}, \tag{10}$$

where a_{sa} and b_{sa} are the least-squares fitted slope and intercept, respectively. We found that the fitted intercept b_{sh} increased slowly with increasing V_{sa} (Table 4), while the intercept of b_{sa} increased significantly with increasing V_{sh} (Table 5). The fitted slope a_{sh} was almost 40 times greater than the fitted slope a_{sa} , which indicated that the sample particle velocity was much more dependent on the sheath flow velocity than the sample flow velocity. This result was attributed to the fact that the sheath flow had a much greater flow rate than the sample flow in the micro-channel.

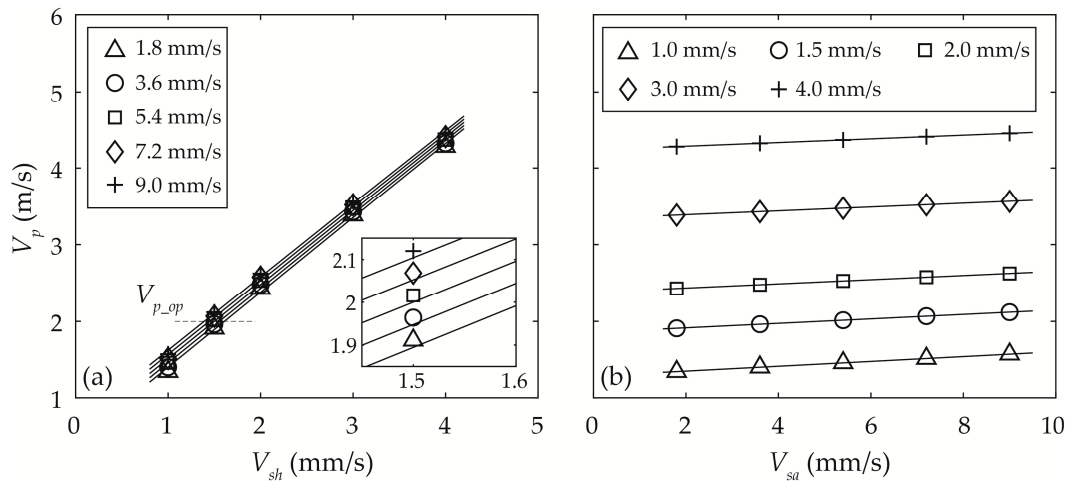


Figure 5. Sample particle velocity V_p as a function of (a) sheath flow velocity V_{sh} at five different sample flow velocities V_{sa} , and (b) V_{sa} at five different V_{sh} . The dashed line in (a) represents the critical particle velocity V_{p_op} (i.e., 2 m/s).

Table 4. The fitted coefficients of sample particle velocity V_p versus sheath flow velocity V_{sh} at five different sample flow velocities V_{sa} .

V_{sa} (mm/s)	a_{sh}	b_{sh}	R^2
1.8	0.9710	0.4379	0.9999
3.6	0.9664	0.4980	0.9999
5.4	0.9624	0.5562	0.9999
7.2	0.958	0.6155	0.9999
9	0.9541	0.6731	0.9999

Table 5. The fitted coefficients of sample particle velocity V_p versus sample flow velocity V_{sa} at five different sheath flow velocities V_{sh} .

V_{sh} (mm/s)	a_{sa}	b_{sa}	R^2
1.0	0.03126	1.295	0.9999
1.5	0.02899	1.859	1
2.0	0.02712	2.381	1
3.0	0.02491	3.339	1
4.0	0.02408	4.238	1

3.3.2. Width of the Sample Particle Stream W_{sa}

Figure 3c,d show that the sample particles were focused around the central axis of the micro-channel for each combination of sample and sheath flow velocities. However, the width of the particle stream W_{sa} , which indicated the distribution range of the sample particles in the micro-channel (i.e., imaging area), changed differently depending on V_{sh} and V_{sa} . W_{sa} decreased with increasing V_{sh} , and the decreasing rate decreased with increasing V_{sh} at each V_{sa} (Figure 6a). In contrast, W_{sa} increased with increasing V_{sa} , but the increasing rate decreased with increasing V_{sa} for each V_{sh} (Figure 6b). Hence, the following general power functions were used to represent W_{sa} as functions of V_{sh} for each V_{sa} and V_{sa} for each V_{sh} :

$$W_{sa}(V_{sh}) = fV_{sh}^g + h, \tag{11}$$

$$W_{sa}(V_{sa}) = fV_{sa}^g + h, \tag{12}$$

where f , g , and h are the least-squares fitted coefficients. The goodness of the fit values are all better than 0.9981 (Tables 6 and 7). The power coefficient g was relatively stable, and smaller and bigger than

0 for Equations (11) and (12) separately. This phenomenon was in good agreement with the trend of W_{sa} changing with V_{sh} (Figure 6a) and V_{sa} (Figure 6b), respectively. In contrast, the coefficient f increased significantly with faster sample velocities V_{sa} for Equation (11) and decreased significantly with faster sheath velocities V_{sh} for Equation (12). These results indicated that a faster sheath flow and a slower sample flow were needed to narrow W_{sa} .

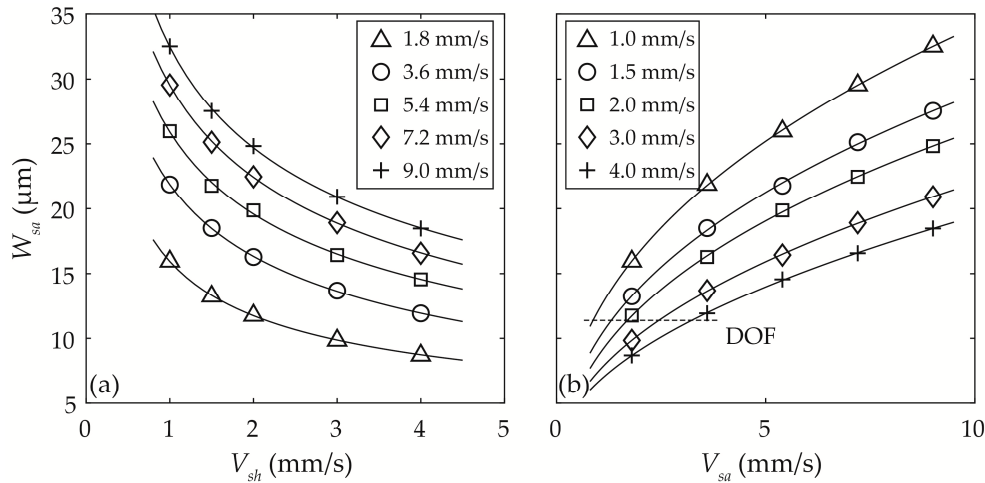


Figure 6. The width of sample particle stream W_{sa} as a function of (a) sheath flow velocity V_{sh} at five different sample flow velocities V_{sa} , and (b) V_{sa} at five different V_{sh} . The dashed line in (b) is half of the depth of field (DOF) of the imaging device (i.e., 11.38 μm).

Table 6. The fitted coefficients of the width of sample particle stream W_{sa} versus sheath flow velocity V_{sh} at five different sample flow velocities V_{sa} .

V_{sa} (mm/s)	f	g	h	R^2
1.8	14.74	-0.4826	1.194	0.9984
3.6	26.65	-0.3364	-4.780	0.9999
5.4	30.82	-0.3316	-4.905	0.9981
7.2	39.71	-0.2841	-10.18	0.9999
9	37.95	-0.3312	-5.471	0.9996

Table 7. The fitted coefficients of the width of sample particle stream W_{sa} versus sample flow velocity V_{sa} at five different sheath flow velocities V_{sh} .

V_{sh} (mm/s)	f	g	h	R^2
1.0	14.27	0.4037	-2.128	0.9999
1.5	12.77	0.3944	-2.831	0.9992
2.0	11.68	0.3953	-3.006	0.9998
3.0	7.725	0.4596	-0.2743	0.9999
4.0	6.006	0.4949	0.6476	0.9999

3.3.3. Optimisation of V_{sh} and V_{sa}

To ensure the working efficiency of the microscopic imaging system and take clear images of the sample particle, the sample particle velocity V_p should be no more than V_{p_op} (i.e., 2 m/s), and the distribution range of the sample particle W_{sa} should be no more than the DOF (i.e., 22.76 μm) in the imaging area of the micro-channel. We investigated the optimal coupling velocities of the sheath and sample flows based on the above theoretical simulation to meet these two requirements concurrently.

We first set V_p to V_{p_op} in Equation (9) to obtain the corresponding V_{sh} for each of the five simulated V_{sa} values (i.e., five crosses on the dashed line with each fitted line in Figure 5a). The five pairs of V_{sh}

and V_{sa} showed that V_{sa} linearly decreased with faster V_{sh} (triangles in Figure 7). Therefore, a linear fit was adopted to represent V_{sa} as a function of V_{sh} :

$$V_{sa} = -36.11V_{sh} + 59.31. \tag{13}$$

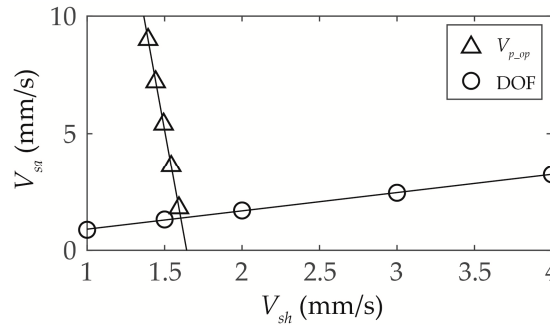


Figure 7. Sample flow velocity V_{sa} as a function of sheath flow velocity V_{sh} when velocity and distribution range of the sample particle are V_{p_op} and DOF, respectively. The intersection of the two fitted lines is the optimised V_{sh} and V_{sa} .

The goodness of the linear fit was better than 0.9999 as indicated by R^2 . We then set W_{sa} to the DOF in Equation (12) to obtain the corresponding V_{sa} for each of the five simulated V_{sh} values (i.e., five crosses on the dashed line with each fitted curve in Figure 6b). V_{sa} linearly increased with faster V_{sh} (circles in Figure 7). Thus, we applied a linear fit to the relationship between V_{sa} and V_{sh} :

$$V_{sa} = 0.7783V_{sh} + 0.1212. \tag{14}$$

The goodness of the linear fitting was better than 0.9995 as indicated by R^2 . Then, we obtained the optimised V_{sh} and V_{sa} , which were represented by the intersection of the two lines determined by Equation (13) and Equation (14) (Figure 7). The theoretical optimised V_{sh} and V_{sa} were 1.6045 and 1.3700 mm/s, respectively, which corresponded to sheath and sample flow rates of 40.9950 $\mu\text{L/s}$ and 1.0755 $\mu\text{L/s}$, respectively.

4. Experimental Verification

4.1. Experiments

Figure 8 shows an experimental prototype of the microscopic imaging system that was built to verify the optimal sample and sheath flow velocities from the above theoretical calculation. The key components were the same as those introduced in Section 2. The sample and sheath flow velocities at the entrance of the flow cell were adjusted with a syringe pump and peristaltic pump, respectively. The CCD camera was focused on the middle of the micro-channel (i.e., imaging area) and covered the entire channel width to monitor the movements of the flows and particles. Three types of water samples were fabricated and used in the experiment. Preliminary examinations showed that the smear of a polystyrene spherical bead (Thermo Fisher Scientific, Inc.) was much more significant than that of real phytoplankton; this was likely due to that the bead behaved like a micro-lens which focused the incident light at its focal point located on the axis passing by the center of the sphere. Thus, water sample 1 was made from polystyrene spherical beads dissolved in deionised water; this was used to mimic phytoplankton in water and examine how the sample particle velocity is affected by the sample and sheath flow velocities. The beads were spherical and had a nominal diameter of 12 μm and density of 1055 kg/m^3 . Water sample 2 was made of seawater containing *Heterosigma akashiwo*, which is a small phytoplankton with a diameter of 8–25 μm . This was used to test the image quality taken by the

prototype with real phytoplankton. Water sample 3 was made with black dye ink to test the width of the sample flow core W_{sa} in the micro-channel.

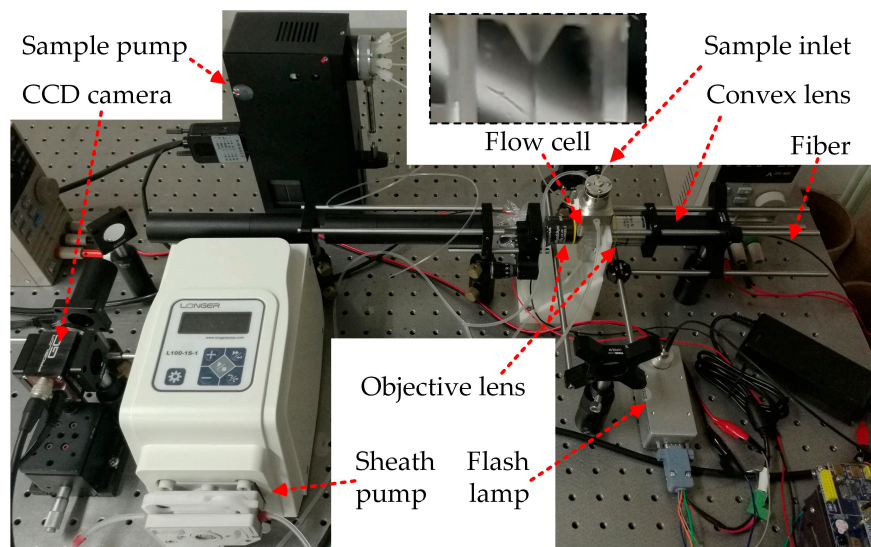


Figure 8. Experimental configuration of the microscopic imaging system. The flow cell is enlarged and shown in the dashed box.

The CCD camera was used to take images of water sample 1 in the micro-channel with varying sample and sheath flow rates to examine their effects on the sample particle velocity. The sample flow rate was set to 1.42, 2.84, 4.26, 5.68, and 7.10 $\mu\text{L/s}$. For each sample flow rate, the sheath flow rate was set to 25.5, 38.2, 51.0, 76.5, and 102 $\mu\text{L/s}$. Therefore, 25 groups of measurements were taken corresponding to these combinations. For each measurement, the CCD camera was set up to collect images at a frequency of 30 Hz. The width of the sample flow core W_{sa} was investigated in a very similar manner, except that sample 3 was used instead of sample 1. We tested the image quality of the prototype with water sample 2 at a sample flow rate of 1.133 $\mu\text{L/s}$ and sheath flow rate of 41.0 $\mu\text{L/s}$, which were the closest to the theoretically optimal flow rates that could be generated by the prototype. Two different sheath flow rates of 25.5 and 76.5 $\mu\text{L/s}$ were also considered for comparison.

4.2. Experimental Results

4.2.1. Smear of Sample Particles

Directly measuring the sample particle velocity in the micro-channel is demanding, and it requires expensive measurement devices. The above simulation had shown that the sample particle velocity in the imaging area was very steady (Figure 3). Alternatively, the smear of the sample particle can be considered proportional to the sample particle velocity; thus, it was used to evaluate the influence of the sample and sheath flow velocities. The measurements of water sample 1 showed that most of the polystyrene beads were imaged clearly (Figure 9). The smear length L_s (i.e., length of the bright tail behind each bead) was quantified by the number of pixels along the horizontal axis passing through the centre of the particle. At each combination of velocities of the sample flow and sheath flow, we randomly selected 20 images and calculated L_s . The results denoted that L_s was relatively stable and the absolute value of the discrepancy was no higher than 10% for each group of 20 images. The discrepancy was probably due to pulsation of the sheath pump and contrast change of the image. We observed that L_s increased significantly with the sample and sheath flow velocities which agreed with the above assumption that L_s was proportional to the sample particle velocity.

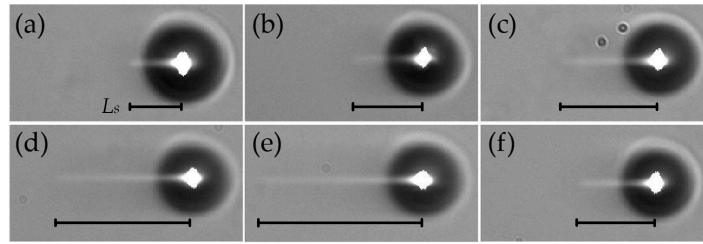


Figure 9. The smear length of water sample 1 L_s at five experimental sheath flow rates of (a) 25.5 $\mu\text{L/s}$, (b) 38.2 $\mu\text{L/s}$, (c) 51.0 $\mu\text{L/s}$, (d) 76.5 $\mu\text{L/s}$, (e) 102 $\mu\text{L/s}$ and (f) the optimised flow rate of 41.0 $\mu\text{L/s}$. The sample flow rate is 1.42 $\mu\text{L/s}$.

To compare the experimental results (i.e., L_s) with the simulation results (i.e., V_p), we normalised each group of measurements as follows:

$$X_{nor} = (X - X_{avr}) / (X_{max} - X_{min}), \tag{15}$$

where X_{nor} is the normalised data, X is the original data, X_{avr} is the average of the group of measurements, and X_{max} and X_{min} are the maximum and minimum, respectively, of the group of measurements. After we normalised L_s , we found that the normalised smear length L_s' increased linearly with increasing V_{sh} and V_{sa} (points with different marker styles in Figure 10). Therefore, L_s' can be represented as the following linear functions of V_{sh} and V_{sa} :

$$L_s'(V_{sh}) = a'_{sh} V_{sh} + b'_{sh'} \tag{16}$$

$$L_s'(V_{sa}) = a'_{sa} V_{sa} + b'_{sa'} \tag{17}$$

where a_{sh}' , b_{sh}' , a_{sa}' , and b_{sa}' are the least-squares fitted coefficients (Tables 8 and 9). The goodness of the linear fitting indicated by R^2 for Equation (17) was not comparable to that of Equation (16), possibly ascribing to that the particle velocity in the micro-channel was dominated by the sheath flow. Similarly, we normalised V_p according to Equation (15) and observed that the normalised sample particle velocity V_p'' also increased linearly with increasing V_{sh} and V_{sa} . As a result, V_p'' can be represented by the following linear functions of V_{sh} and V_{sa} (solid lines in Figure 10):

$$V_p''(V_{sh}) = a''_{sh} V_{sh} + b''_{sh'} \tag{18}$$

$$V_p''(V_{sa}) = a''_{sa} V_{sa} + b''_{sa'} \tag{19}$$

where a_{sh}'' , b_{sh}'' , a_{sa}'' , and b_{sa}'' are the least-squares fitted coefficients (Tables 8 and 9). The goodness of the linear fitting are all better than 0.9984. Figure 10a shows that L_s' (points with different marker styles) was uniformly distributed on both sides of each fitted V_p'' (solid line) for each V_{sa} . Meanwhile, the fitted slope a_{sh}' was very close to the fitted slope of a_{sh}'' (Table 8). Similarly, the general trend of L_s' with V_{sa} also agreed well with that of V_p'' with V_{sa} for each V_{sh} (Figure 10b, Table 9). The root mean square error (RMSE) between L_s' and V_p'' was no higher than 0.02 for each group of V_{sh} at each V_{sa} (Figure 10a) or each group of V_{sa} at each V_{sh} (Figure 10b), which indicated that the laboratory experiment agreed well with theoretical simulation.

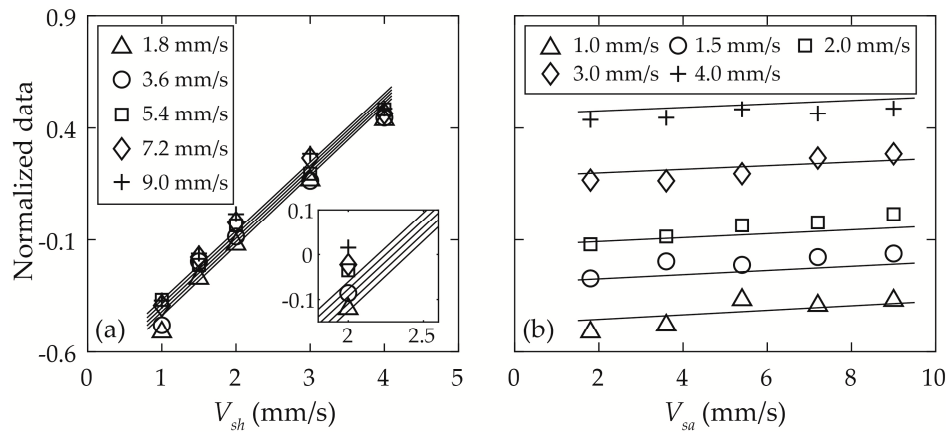


Figure 10. Normalized smear length L_s' (the points with different marker styles) and normalized particle velocity V_p'' (the solid lines) as a function of (a) sheath flow velocity V_{sh} at five different sample flow velocities V_{sa} , and (b) V_{sa} at five different V_{sh} .

Table 8. The fitted coefficients of L_s' and V_p'' versus sheath flow velocity V_{sh} at five different sample flow velocities V_{sa} .

V_{sa} (mm/s)	L_s' (Experiment)			V_p'' (Simulation)		
	a_{sh}'	b_{sh}'	R^2	a_{sh}''	b_{sh}''	R^2
1.8	0.3069	-0.7664	0.9895	0.3129	-0.7514	0.9984
3.6	0.2899	-0.6976	0.9776	0.3114	-0.7320	0.9985
5.4	0.2789	-0.6286	0.9961	0.3101	-0.7133	0.9986
7.2	0.2820	-0.6211	0.9831	0.3087	-0.6942	0.9987
9	0.2816	-0.5969	0.9813	0.3075	-0.6756	0.9987

Table 9. The fitted coefficients of L_s' and V_p'' versus sample flow velocity V_{sa} at five different sheath flow velocities V_{sh} .

V_{sh} (mm/s)	L_s' (Experiment)			V_p'' (Simulation)		
	a_{sa}'	b_{sa}'	R^2	a_{sa}''	b_{sa}''	R^2
1.0	0.02075	-0.5371	0.7647	0.01008	-0.4751	0.9999
1.5	0.01336	-0.2763	0.7921	0.009341	-0.2933	1
2.0	0.01864	-0.1504	0.9760	0.008741	-0.1253	1
3.0	0.01864	0.1148	0.8940	0.008026	0.1834	1
4.0	0.006681	0.4275	0.7177	0.007761	0.4731	1

Figure 11 show the images of water sample 2 taken by the prototype at three different sheath flow rates. The smear of *H. akashiwo* was not as sensitive as that of the polystyrene bead to different shear flow velocities. At the theoretically optimal sample and sheath flow rates, the smear of the *H. akashiwo* was not very significant, and the shape of the phytoplankton could be clearly identified (Figure 11b). In contrast, with the faster sheath velocity, the shape of the phytoplankton became blurred (Figure 11c). The results indicated that the theoretically optimal sample and sheath flow rates obtained in this study are applicable to the microscopic imaging system.

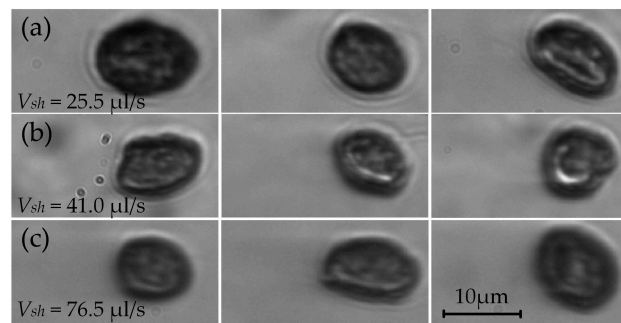


Figure 11. Images of water sample 2 at three different sheath flow rates of (a) 25.5 $\mu\text{L/s}$, (b) 41.0 $\mu\text{L/s}$ (i.e., the closest to the optimised sheath flow rate), and (c) 76.5 $\mu\text{L/s}$. The sample flow rate is 1.133 $\mu\text{L/s}$ (i.e., the closest to the optimised sample flow rate). The three photos in each row are taken under the same sample and sheath flow rates.

4.2.2. Width of the Focused Sample Flow Stream W_{sa}

Figure 12 shows that water sample 3 was precisely focused into a narrow stream in the micro-channel and passed through the imaging area very smoothly with each combination of the sample and sheath flow velocities. The focused stream was not at the central axis of the micro-channel because the fine needle used to discharge the sample flow was not installed exactly at the central axis of the conical channel. The width of the focused stream W_{sa} changed with the sample flow velocity V_{sa} and sheath flow velocity V_{sh} . W_{sa} decreased gradually with increasing V_{sh} , and the decreasing rate decreased with increasing V_{sh} for each V_{sa} (Figure 13a). The experimental relationship between W_{sa} and V_{sa} agreed with that in the theoretical simulation: W_{sa} increased with V_{sa} , but the increasing rate decreased with increasing V_{sa} for each V_{sh} (Figure 13b). Each group of experimental measurement data (discrete points in Figure 13) was uniformly distributed on both side of each fitted curve (solid curves in Figure 13) derived from the theoretical simulation in Section 3. The absolute value of the discrepancy between the theoretically calculated value and the experimental value was no higher than 6% for each group of sheath and sample flow velocities, which meant that our model could properly predict the width of the focused sample flow stream in the micro-channel.

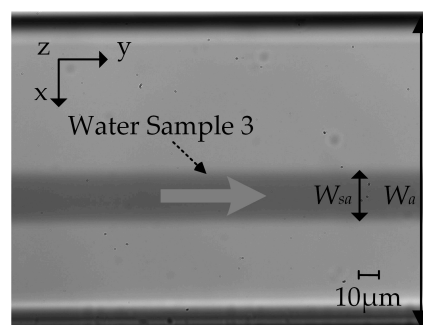


Figure 12. Images of sample 3 at the sheath flow rate of 25.5 $\mu\text{L/s}$ and sample flow rate of 2.84 $\mu\text{L/s}$.

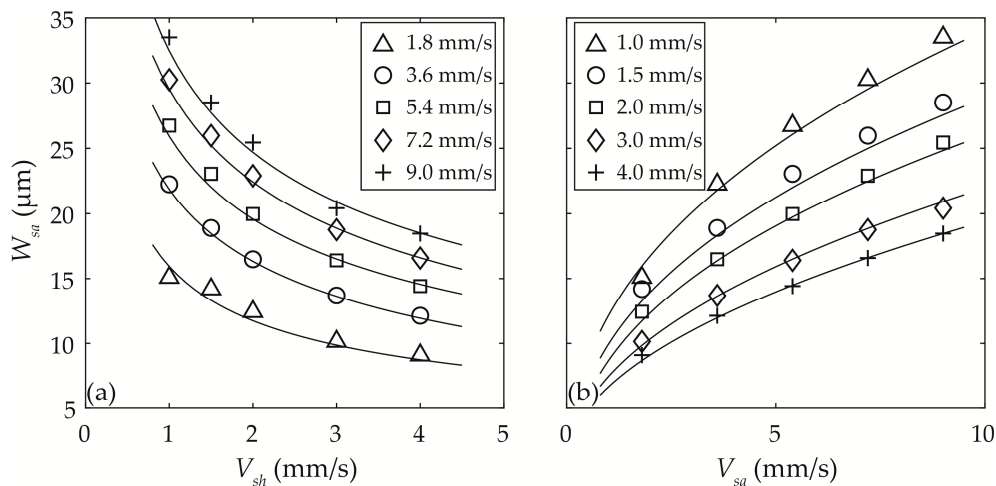


Figure 13. The width of sample particles stream W_{sa} as a function of (a) sheath flow velocity V_{sh} at five different sample flow velocities V_{sa} , and (b) V_{sa} at five different V_{sh} . In this figure, the discrete points with different marker styles derive from the experimental measurement. Whereas, the solid curves derive from the theoretical simulation conducted in Section 3, which are the same as those shown in Figure 6.

5. Conclusions

The optimal coupling velocities of the sample and sheath flows of a microscopic imaging system were investigated to ensure its working efficiency and imaging quality. The hydrodynamic focusing subsystem was analysed and modelled with a symmetrical 3D model. The changes in the velocity V_p and distribution range W_{sa} of the sample particle in the imaging area with the sample flow velocity V_{sa} and sheath flow velocity V_{sh} were theoretically simulated. The results indicated that V_p increased with both V_{sa} and V_{sh} . The slope (i.e., increasing rate) of V_p was much bigger with increasing V_{sh} than with increasing V_{sa} , which indicates that V_p is much more dependent on V_{sh} than on V_{sa} . W_{sa} decreased with increasing V_{sh} , and the decreasing rate decreased with increasing V_{sh} . However, W_{sa} increased with V_{sa} , and the increasing rate decreased with increasing V_{sa} . These results were used to obtain the theoretically optimal coupling velocities of the sample and sheath flows. A prototype of the microscopic imaging system was built, and the changes in V_p and W_{sa} with different V_{sa} and V_{sh} were experimentally examined. The experimental results agreed well with the theoretical results. This indicates that the optimal coupling velocities of the sample and sheath flows are applicable to the microscopic imaging system.

Although the results obtained in this study are promising, several aspects might benefit from improvement. First, we investigated the optimal coupling velocities of the sample and sheath flows in the micro-channel using microparticle as small as 12 μm . Whereas, the size range of the sample particle for the microscopic imaging system was 10–150 μm . The size change of the sample particle might lead to the variation of the particle Raynor number, which may lead to variation of the particle motion in the micro-channel and the optimal coupling velocities of the sample and sheath flows. Even though the influence of particle size may not be significant to this study [21], it should be investigated in more detail in future for rigor. Second, the direct measurement of velocities of the sample particle and flow in the micro-channel will be more intuitional to reflect the influence of velocities of the sample flow and sheath flow, and more convenient for the investigation of the optimal coupling velocities of the sample flow and sheath flow. Finally, fluorescent microbeads will be considered in future to examine the smearing effect of the beads under different velocities of the sample flow and sheath flow [22].

Author Contributions: Conceptualization, H.W. and X.W.; methodology, D.H., H.Z., and K.G.; software, D.H. and K.G.; investigation, D.H. and K.G.; resources, Z.Y. and J.C.; data curation, D.H. and H.W.; writing—original draft preparation, D.H. and H.W.; writing—review and editing, X.W., Z.Y., and J.C.; supervision, H.W. and X.W.; project administration, Y.C. All authors have read and agreed to the published version of the manuscript.

Funding: This research was funded by Joint Zhoushan City and Zhejiang University Cooperation Project (Grant No. 2019C82089), National Natural Science Foundation of China (Grant No. 41976218), and the National Key Research and Development Program of China (Grant No. 2017YFC0307703).

Acknowledgments: The authors thank Mengmeng Tong (Ocean College, Zhejiang University) for providing phytoplankton during the experimental verification.

Conflicts of Interest: The authors declare no conflict of interest.

References

1. Altschuler, S.J.; Wu, L.F. Cellular heterogeneity: Do differences make a difference? *Cell* **2010**, *141*, 559–563. [[CrossRef](#)] [[PubMed](#)]
2. Das, D.; Biswas, K.; Das, S. A microfluidic device for continuous manipulation of biological cells using dielectrophoresis. *Med. Eng. Phys.* **2014**, *36*, 726–731. [[CrossRef](#)] [[PubMed](#)]
3. Jiang, H.; Weng, X.; Li, D. A novel microfluidic flow focusing method. *Biomicrofluidics* **2014**, *8*, 054120. [[CrossRef](#)]
4. Collins, D.J.; Morahan, B.; Garcia-Bustos, J. Two-dimensional single-cell patterning with one cell per well driven by surface acoustic waves. *Nat. Commun.* **2015**, *6*, 1–11. [[CrossRef](#)]
5. Ha, B.H.; Lee, K.S.; Jung, J.H. Three-dimensional hydrodynamic flow and particle focusing using four vortices Dean flow. *Microfluid. Nanofluidics* **2014**, *17*, 647–655. [[CrossRef](#)]
6. Versaci, M.; Palumbo, A. Magnetorheological fluids: Qualitative comparison between a mixture model in the extended irreversible thermodynamics framework and an Herschel—Bulkley experimental elastoviscoplastic model. *Int. J. Non Linear Mech.* **2020**, *118*, 103288. [[CrossRef](#)]
7. Luo, T.; Fan, L.; Zhu, R. Microfluidic single-cell manipulation and analysis: Methods and applications. *Micromachines* **2019**, *10*, 104. [[CrossRef](#)]
8. Hamilton, E.S.; Ganjalizadeh, V.; Wright, J.G. 3D Hydrodynamic Focusing in Microscale Optofluidic Channels Formed with a Single Sacrificial Layer. *Micromachines* **2020**, *11*, 349. [[CrossRef](#)]
9. Wang, Q.; Yuan, D.; Li, W. Analysis of hydrodynamic mechanism on particles focusing in micro-channel flows. *Micromachines* **2017**, *8*, 197. [[CrossRef](#)]
10. Wang, X.; Zandi, M.; Ho, C.C. Single stream inertial focusing in a straight microchannel. *Lab A Chip* **2015**, *15*, 1812–1821. [[CrossRef](#)]
11. Panwar, N.; Song, P.; Tjin, S.C. Sheath-assisted hydrodynamic particle focusing in higher Reynolds number flows. *J. Micromechanics Microengineering* **2018**, *28*, 105018. [[CrossRef](#)]
12. Chiu, Y.J.; Cho, S.H.; Mei, Z. Universally applicable three-dimensional hydrodynamic microfluidic flow focusing. *Lab A Chip* **2013**, *13*, 1803–1809. [[CrossRef](#)] [[PubMed](#)]
13. Mao, X.; Lin, S.C.S.; Dong, C. Single-layer planar on-chip flow cytometer using microfluidic drifting based three-dimensional (3D) hydrodynamic focusing. *Lab A Chip* **2009**, *9*, 1583–1589. [[CrossRef](#)] [[PubMed](#)]
14. Lee, G.B.; Hung, C.I.; Ke, B.J. Hydrodynamic Focusing for a Micromachined Flow Cytometer. *J. Fluids Eng.* **2001**, *123*, 672. [[CrossRef](#)]
15. Lee, G.B.; Chang, C.C.; Huang, S.B. The hydrodynamic focusing effect inside rectangular microchannels. *J. Micromechanics Microengineering* **2006**, *16*, 1024. [[CrossRef](#)]
16. Oakey, J.; Applegate, R.W.; Arellano, E. Particle focusing in staged inertial microfluidic devices for flow cytometry. *Anal. Chem.* **2010**, *82*, 3862–3867. [[CrossRef](#)]
17. Zhao, J.; You, Z. Microfluidic hydrodynamic focusing for high-throughput applications. *J. Micromechanics Microengineering* **2015**, *25*, 125006. [[CrossRef](#)]
18. Stiles, T.; Fallon, R.; Vestad, T. Hydrodynamic focusing for vacuum-pumped microfluidics. *Microfluid. Nanofluidics* **2005**, *1*, 280–283. [[CrossRef](#)]
19. Cornish, R.J. Flow in a pipe of rectangular cross-section. *Proc. R. Soc. Lond. Ser. A Contain. Pap. A Math. Phys. Character* **1928**, *120*, 691–700.
20. Olson, R.; Sosik, H. A submersible imaging-in-flow instrument to analyze nano- and microplankton: Imaging FlowCytobot. *Limnol. Oceanogr. Methods* **2007**, *5*. [[CrossRef](#)]

21. Carlo, D.; Edd, F.; Humphry, J.; Stone, H.A.; Toner, M. Particle Segregation and Dynamics in Confined Flows. *Phys. Rev. Lett.* **2009**, *9*, 102. [[CrossRef](#)] [[PubMed](#)]
22. Hayat, Z.; Abed, A. High-Throughput Optofluidic Acquisition of Microdroplets in Microfluidic Systems. *Micromachines* **2018**, *9*, 183. [[CrossRef](#)] [[PubMed](#)]



© 2020 by the authors. Licensee MDPI, Basel, Switzerland. This article is an open access article distributed under the terms and conditions of the Creative Commons Attribution (CC BY) license (<http://creativecommons.org/licenses/by/4.0/>).